Materials LAB

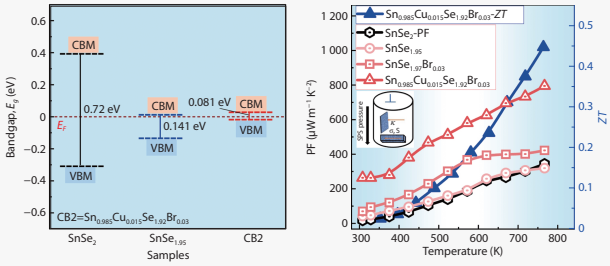
RESEARCH ARTICLE

Materials Lab 2024, 3, 230023

Synergistic optimization of thermoelectric performance in $SnSe_2$ through Co-doping: anionic vacancy formation and band engineering

Mohammad Nisar, Wenning Qin, Junze Zhang, Zhuanghao Zheng, Fu Li, Guangxing Liang, Ping Fan and Yue-Xing Chen*

$SnSe_2$ is a layered crystal structure material that is abundant in the Earth's crust and considered non-toxic. However, its thermoelectric properties are anisotropic due to the differences in its interlayer and intralayer electrical and thermal transport properties. The intrinsically poor thermoelectric performance of $SnSe_2$ can be attributed to its lower electrical transport properties in its pristine condition. To address this, we developed a method involving combined mechanical alloying (MA) and spark plasma sintering (SPS) to synthesize n-type Sn-rich Cu-Br co-doped $SnSe_2$ polycrystals. Optimization of Sn enrichment facilitated superior material selection for subsequent doping. The resulting substitutional doping induced a substantial rise in carrier concentration, leading to improved thermoelectric performance. Notably, the power factor displayed a significant increase, reaching approximately 795 μW m^{-1} K^{-2} at 765 K through Cu-Br co-doping. Furthermore, density functional theory (DFT) analysis elucidated a reduced bandgap and increased degeneracy within the electronic band structure and density of states, affirming the enhancement of thermoelectric properties in Cu-Br co-doped Sn-rich $SnSe_2$ polycrystals. Finally, a maximum figure of merit (*ZT*) value of 0.46 was achieved at 765 K for the $Sn_{0.985}Cu_{0.015}Se_{1.92}Br_{0.03}$ sample, perpendicular to the SPS pressing direction, which was nearly threefold higher than the pure $SnSe_{1.95}$. This compelling outcome highlights the improved thermoelectric performance of the co-doped $SnSe_2$ polycrystals.



The thermoelectric (TE) effect presents a highly promising solution for the recovery of waste heat by converting thermal energy into electrical energy. TE devices offer a multitude of advantages, including reliable and vibration-free operation, as well as being emission-free, making them an excellent choice for a sustainable carbon-neutral renewable energy conversion system[1-4]. Therefore, it is no surprise that in the past two decades, numerous researchers in the TE community have focused their efforts on improving the energy conversion efficiencies of TE materials by manipulating their atomic, crystallographic, and microstructural properties[5-7]. With these improvements, the potential for TE technology to provide an efficient and environmentally friendly source of energy continues to grow. Thermoelectric materials utilize a fascinating physical phenomenon called thermoelectricity, which enables the direct conversion of heat into electricity, and vice versa[8]. Indeed, TE materials have the potential to play a significant role in mitigating the conflict between depleting fossil fuels and increasing energy demands[9-12]. A dimensionless figure of merit (*ZT*) can evaluate the aptitude of energy conversion of thermoelectric materials, having the formula $ZT = S^2\sigma T/(\kappa_{ele}+\kappa_{latt})$, where T is the absolute temperature, S is the Seebeck coefficient, σ is the electrical conductivity, κ_{ele} represents the electronic thermal conductivity, κ_{latt} is the lattice thermal conductivity, and $S^2\sigma$ is referred to as the power factor (PF)[13, 14], furthermore, it's important to consider that the κ_{tot} is equal to the sum of the electronic (κ_{ele}) and lattice (κ_{latt}) thermal conductivities. However, the power factor (PF), Seebeck coefficient (S), electrical conductivity (σ), and thermal conductivity (κ) are interdependent, making it challenging to simultaneously increase the PF and reduce the thermal conductivity. This is because factors that improve the PF, such as the density of states and carrier mobility, also affect the electronic and phonon transport properties that contribute to thermal conductivity[15, 16]. Therefore, researchers face the task of optimizing the electronic and phonon transport properties of the material to achieve a balance between the PF and thermal con-

Shenzhen Key Laboratory of Advanced Thin Films and Applications, Key Laboratory of Optoelectronic Devices and Systems of Ministry of Education and Guangdong Province, College of Physics and Optoelectronic Engineering, Shenzhen University, Shenzhen 518060, China

* Corresponding author, E-mail: chenyx@szu.edu.cn

Received 23 May 2023; Accepted 26 June 2023; Published online

© 2024 The Author(s). *Materials Lab* published by Lab Academic Press

DOI: 10.54227/mlab.20230023

ductivity. To overcome this challenge, various techniques have been explored, such as nanostructuring, doping, and band engineering, to manipulate the electronic and phonon transport properties of the material. These techniques have shown promise in achieving significant improvements in the *ZT* value, leading to more efficient energy conversion and a wide range of potential applications in sustainable energy technology[17-19].

Layered materials possess distinct characteristics arising from the anisotropy between interlayer and intralayer transport properties. This property enables customizable modifications, leading to tailored properties suitable for various applications. These materials hold great promise in diverse fields such as energy, electronics, and catalysis[20, 21]. Over the past two decades, Sn-based layered chalcogenides have been extensively studied by thermoelectric researchers, leading to significant improvements in our understanding of their thermoelectric properties[22-25]. $SnSe_2$ is a promising medium-temperature (300-830 K) thermoelectric material that has been extensively studied due to its unique properties. It is an n-type intrinsic semiconductor[26] with a relatively wide bandgap of around 1.1 eV, high valence/conduction band degeneracy, and high Seebeck coefficient[27, 28]. Additionally, $SnSe_2$ is affordable and non-toxic, making it an environmentally friendly material that has gained much attention in the past decade. It adopts a hexagonal CdI_2-type layered structure with stable two-dimensional Se-Sn-Se crammed interlayers weakly coupled by van der Waals forces. Another study found that $SnSe_2$ exhibits significant anisotropy in transport coefficients along both parallel and perpendicular directions[25, 29]. Its unique layer-dependent structure and electronic properties have led to extensive investigations to improve the performance of electronic devices, including photo-detectors, transistors, and energy storage humidity sensors[30, 31]. The layered structure of $SnSe_2$ results in inherently low thermal conductivity and robust anisotropic phonon-transport properties. Similar to SnSe, $SnSe_2$ exhibits higher thermal conductivity in polycrystalline form and lower thermal conductivity in single crystals, which can be enhanced through doping[11, 32, 33]. These notable properties of $SnSe_2$ make it a promising candidate for thermoelectric applications. As a result, there has been increasing interest in investigating and improving its thermoelectric performance. However, the options for enhancing thermoelectric properties in materials with a similar crystal structure to SnSe2 are currently limited to techniques focused on reducing lattice thermal conductivity through nanostructuring. Some of these techniques include compacting nanoparticles that have been synthesized colloidal[34], cautiously packing nanoplatelets[27], and embedding dense nanoscale precipitates into $SnSe_2$ nanopowders[35]. Nonetheless, it is difficult to achieve a low lattice thermal conductivity in $SnSe_2$ similar to that of SnSe because the Sn atoms in $SnSe_2$ form an almost perfect octahedron with Se ligands, resulting in isotropic Sn-Se bond distances. As a result, $SnSe_2$ only exhibits a moderately low thermal conductivity[11, 27]. Although various studies have attempted to enhance the thermoelectric properties of $SnSe_2$, little research has been conducted on the effect of anionic vacancy engineering within a broad range. Similarly, while antisite defects techniques have also been performed on both Sn and Se sites, as well as Cu intercalation,[26, 36-39] but combination of anionic vacancy engineering and co-doping on both sites of $SnSe_2$ has been rarely explored for its thermoelectric performance.

In this work, we first obtained the optimal value of Sn-enrichment in n-type $SnSe_2$ polycrystals. Then introduced Cu and Br on Sn and Se sites, respectively, to improve and optimize its thermoelectric properties by mechanical alloying combined with a Sparkle plasma sintering technique, as illustrated by Fig. S1 of the supporting information. A broad range of Cu and Br dopants have been added to Sn-rich $SnSe_2$ {$Sn_{1-x}Cu_xSe_{2-y}Br_y$ ($0 \le x \le 0.035$, $0 \le y \le 0.07$)} to optimize the thermoelectric (TE) properties of the material in both in-plane and out of plane directions. The addition of Br and Cu dopants acted as donors and lead to increase in concentration of electrons and optimized power factor to 795 $\mu Wm^{-1}K^{-2}$ at 765 K. The ionic radii of Cu/Br are compatible with those of Sn/Se and Se/Br atoms, respectively, which prevented any potential disruption to the host material's crystal structure and resulted in an increased carrier concentration. Our results showed that the optimized Se-rich condition and Cu/Br co-doping resulted in a higher carrier concentration and a lower thermal conductivity compared to pure $SnSe_2$. This led to a significant improvement in the power factor of the material, which is a key parameter for thermoelectric performance and is directly proportional to the square of Seebeck coefficient and electrical conductivity. Therefore, our findings suggest that Cu/Br co-doped Sn-rich $SnSe_2$ has the potential to be a promising thermoelectric material. We also performed DFT simulations to investigate the electronic structure, which further corroborated our experimental findings.

Experimental details

The temperature gradient technique was employed to fabricate large polycrystalline samples of undoped and Cu-Br co-doped $SnSe_2$. To this end, highly pure powders of Sn (5N), Se (5N), and $CuBr_2$ (5N) with purities of 99.99%, 99.99%, and 99.95%, respectively, were used as starting materials. The powders were weighed according to the nominal compositions $Sn_{1-x}Cu_xSe_{2-y}Br_y$ (x = 0, 0.01, 0.015, 0.025, 0.035, y = 0.02, 0.03, 0.05, 0.07) in a vacuum glove box. For convivence the Cu-Br co-doped samples were named with increasing dopant contents as CB1, CB2, CB3 and CB4. The stoichiometric powder mixtures were then thoroughly homogenized and sealed in a quartz tube under vacuum (<10^{-3} Pa). The sealed tube was then heated at 1073 K for 24 h and rapidly cooled to room temperature by furnace quenching. Next, the synthetic $Sn_{1-x}Cu_xSe_{2-y}Br_y$ samples were milled for 2 hours at 200 r min^{-1} in a ball mill, and the resulting powder was pressed into cylindrical pellets with dimensions of 13.2 × 2 mm^3 using a spark plasma sintering (SPS) equipment. The pellets were sintered at 723 K for 5 min under an axial pressure of 50 MPa. The resulting cylindrical-shaped ingots were then obtained by cutting the pellets. The thermal conductivity and electrical properties of the samples were measured along the parallel and perpendicular directions of the SPS pressing to enable proper characterization.

To determine the densities of the SPS-sintered samples, the Archimedes' principle was employed. The crystal structure of

DOI: 10.54227/mlab.20230023

the samples was analyzed using a D/max-RB diffractometer (Rigaku, Tokyo, Japan) with Cu Kα radiation (λ = 1.54 Å) operating at 40 kV and 40 mA, with a continuous examination rate of 4° min^{-1}. The lattice constants were obtained through step-scan X-ray diffraction (XRD) with a step width of 0.02°, utilizing the least square method. Prior to the step-scan XRD, the surfaces of the bulk samples were finely polished to ensure accurate X-ray peak readings. The morphological characteristics of the samples were investigated using a field emission scanning electron microscopy (FE-SEM) instrument (LEO 153, Germany).

The ZEM-3 Seebeck coefficient and electrical resistivity measuring apparatus (Ulvac-RiKo, Japan) was used to measure the Seebeck coefficient and electrical resistivity of the samples as a function of temperature, from 308 K to 767 K. The Hall coefficients were obtained at room temperature using the van der Pauw technique under a universal magnetic field of 0.50 T, utilizing the HL5500PC instrument (Nanometrics). The thermal diffusivity was determined under argon flow using the laser flash diffusivity method (LFA467, Netzsch, Germany). The carrier concentration (n) and carrier mobility (μ) were calculated using the equations $n = 1/(eR_H)$ and $\mu = 1/(ne\rho)$, respectively, where e is the charge of an electron, and R_H is the Hall coefficient obtained using a four-probe method. The total thermal conductivity was estimated using the expression $\kappa_{tot} = dC_pD$, where d, Cp, and D are the density, specific heat, and thermal diffusivity, respectively. The specific heat (Cp) value was obtained from the literature[40].

Theoretical details

The electronic band structures and density of states (DOS) for $Sn_{1-x}Cu_xSe_{1.95-y}B_y$ (where x = 0, 0.01, 0.015, 0.025, 0.035 and y = 0.02, 0.03, 0.05, 0.07) were meticulously calculated to gain a deeper understanding of the material's properties. This was achieved using the advanced Vienna Ab Initio Simulation Package (VASP) within the framework of density functional theory (DFT)[41, 42]. The calculations were carried out using plane-wave pseudopotential formalism and the electron-ion interaction was modelled by exploiting the projector-augmented wave (PAW)[43] technique for Sn ($4d^{10}5s^25p^2$), Se ($4s^24p^2$), Br ($4s^23d^14p^5$), and Cu ($3d^{10}4s^1$) atoms. To ensure the accuracy of the results, the wavefunction's cut-off energy was set to 600 eV, and the generalized gradient approximations (GGA)[44] with the Perdew-Burke-Ernzerhof potential (PBE)[45] were used for the exchange-correlation function. To optimize the crystal structures, the Hellmann-Feynman forces on each atom were minimized to below 1×10^{-6} eV Å^{-1}. Moreover, the energy convergence criterion was set to 1×10^{-7} eV. The supercells of 4×4×2, consisting of 32 Sn and 64 Se sites, were employed to model all structures. In the first step of the calculation, a self-consistent field (SCF) calculation with a Monkhorst-Pack k-point mesh of 6×6×3 was performed. Subsequently, the k-point mesh was increased to 8×8×4 for the calculation of the density of states. To plot the electronic energy bands, a 384 k-point grid was employed.

Results and discussions

Mechanical alloying (MA) and spark plasma sintering (SPS) techniques were employed to synthesize high-quality, n-type Sn-rich polycrystalline $SnSe_2$. The anisotropic characteristics of $SnSe_2$, which stem from its layered structure, were investigated in both the parallel and perpendicular directions to the SPS pressing process. Additionally, Cu-Br onsite co-doping has been achieved, with Cu replacing Sb atoms and Br replacing Se atoms. Fig. 2a and 1e present X-ray diffraction (XRD) patterns of Cu-Br co-doped $SnSe_{1.95}$ samples synthesized along parallel and perpendicular directions to the SPS pressing. For convenience we will denote the doped samples, $Sn_{1-x}Cu_xSe_{1.95-y}B_y$ (where x = 0.01, 0.015, 0.025, 0.035 and y = 0.02, 0.03, 0.05, 0.07), as CB1, CB2, CB3 and CB4 respectively in the work. The diffraction peaks indicate that the synthesized samples are in a hexagonal phase, consistent with the JCPDS data standard card (JCPDS No. 38-1055) and previous research[36]. Fig. 1b, d shows that the major diffraction peak of $SnSe_{1.95}$ shifts towards higher 2θ with increasing Br and Cu contents, but slightly shifts back at x = 0.025 and y = 0.03 in both directions to the SPS pressing. The lattice parameters were estimated using Bragg's law and the expression of d spacing, d_{hkl}. The observed peak shift can be ascribed to alterations in the crystal structure of the material induced by the integration of dopant atoms. These dopant atoms possess the capability to distort the lattice owing to disparities in atomic dimensions, electronic characteristics, or chemical bonding. Consequently, the diffraction peak experiences a displacement towards either higher or lower angles. At elevated dopant concentrations, the lattice undergoes a reorganization process aimed at minimizing strain, which ultimately results in the peak returning closer to its initial position. The refined lattice parameters of $Sn_{1-x}Cu_xSe_{1.95-y}Br_y$ samples were achieved by Rietveld refinement using X-ray diffraction data. The lattice parameters of the a = b, c axes improve with increasing Cu-Br co-doping. After a certain doping contents, the lattice parameters shortened again which also agrees with patterns of major diffraction peak shifts, as shown in Fig. 1c. For example, the lattice parameters of the a-axis $SnSe_{1.95}$, CB1, CB2, CB3 and CB4 samples are approximately 3.794, 3.799, 3.803, 3.794 and 3.793 Å, respectively.

The X-ray diffraction (XRD) pattern exhibits a noticeable shift in the position of the prominent diffraction peak. At lower doping concentrations, the peak shifts towards a higher angle, followed by a shift back towards a lower angle at higher doping concentrations. This behavior can be attributed to the alterations in the crystal structure and lattice parameters induced by the presence of Cu and Br dopants. The incorporation of Cu and Br dopants involves the substitution of some Sn and Se atoms within the crystal lattice. This substitution leads to changes in the crystal structure and lattice parameters. Specifically, at lower doping concentrations, the Cu and Br dopants occupy the interstitial sites within the $SnSe_2$ lattice. This occupation results in lattice expansion and an increase in the lattice parameter. This expansion causes a shift in the major diffraction peak towards a higher angle in the XRD pattern. However, at higher doping concentrations, the Cu and Br dopants also substitute some of the Sn and Se atoms in the lattice, leading to a contraction of the lattice and a decrease in the lattice parameter. This contraction causes the major diffraction peak to shift back towards a lower angle in the XRD pattern.

DOI: 10.54227/mlab.20230023

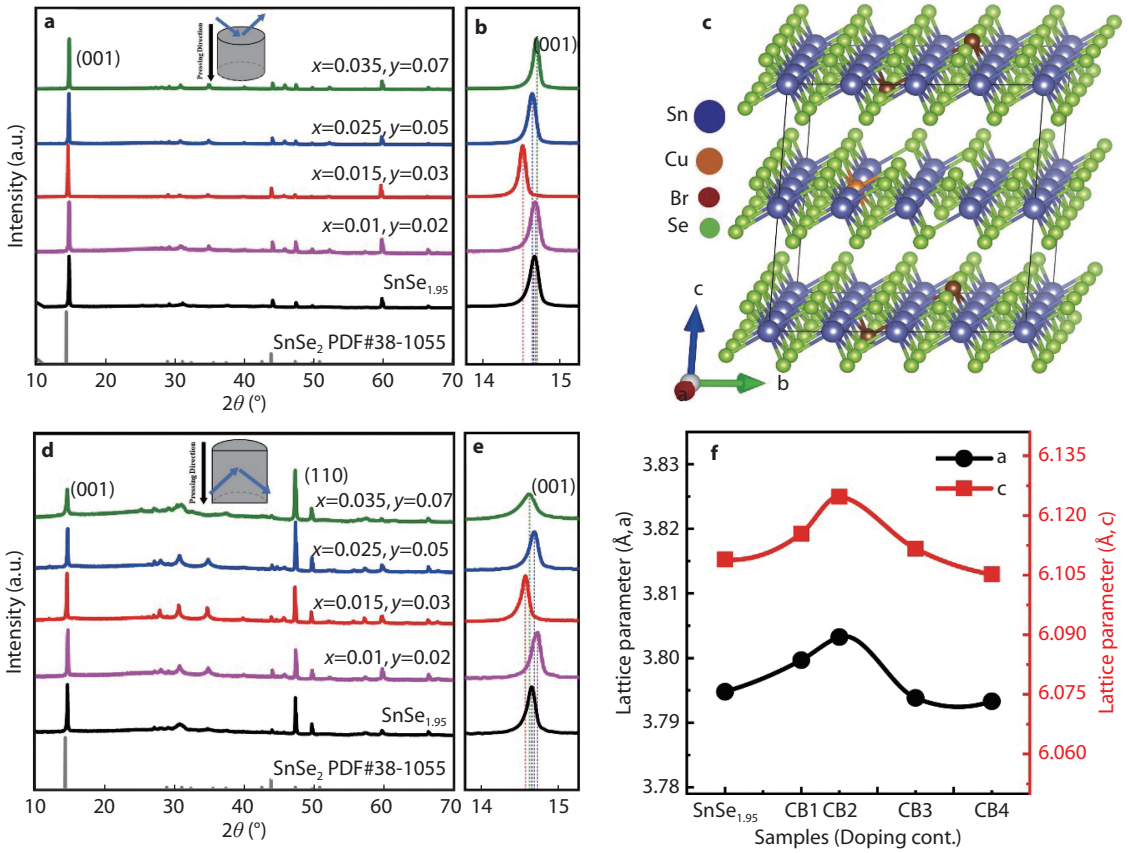


Fig. 1 XRD patterns and of $Sn_{1-x}Cu_xSe_{1.95-y}Br_y$ ($0 \le x \le 0.035$ and $0 \le y \le 0.07$) samples **a, b** along the perpendicular direction, **d, e** along a parallel direction to the SPS pressing. **c** Schematic of Cu-Br co-doped $SnSe_{1.95}$ crystal structure consisting of the $SnSe_6$ octahedral layers. **f** Lattice constants (a = b, c) of $Sn_{1-x}Cu_xSe_{1.95-y}Br_y$ samples.

The field emission scanning electron microscopy (FE-SEM) images provide vivid insights into the surface topography and lamellar microstructural features of $Sn_{1-x}Cu_xSe_{1.95-y}Br_y$ polycrystals, manifesting along both the parallel and perpendicular axes of spark plasma sintering (SPS) pressing. The evidence supporting these statements is presented in Fig. 2a-f and Supplementary Fig. S2, as described in the supporting information. Notably, the field emission scanning electron microscopy (FE-SEM) analysis allows for the visualization of the structural morphology, revealing distinct crystallographic domains within the synthesized polycrystalline samples. Additionally, Fig. 2g-j presents energy-dispersive X-ray spectroscopy (EDS) images of a representative sample (CB2). These EDS elemental mapping images demonstrate a uniform distribution of Cu and Br atoms throughout the scanned areas, similar to that of Sn and Se. This implies the successful incorporation of Cu and Br dopants into the $SnSe_2$, which is conducive to tuning the electronic and thermoelectric properties of the material.

The search for high-performance thermoelectric materials has gained momentum in recent years, with $SnSe_2$ being a promising candidate due to its excellent thermoelectric properties. However, a factor that can significantly affect the thermoelectric properties of $SnSe_2$ is the presence of Se vacancies, which are locations where Se atoms are missing from the crystal structure. Increasing Se vacancies in $SnSe_2$ can lead to several changes in its thermoelectric properties: $SnSe_2$ is an intrinsic semiconductor, meaning it has a relatively low electrical conductivity in its pristine form. However, the introduction of a certain number of Se vacancies can create defects in the crystal structure, which acts as charge carriers and increase the electrical conductivity. The additional charge carriers provided by Se vacancies enhances the overall electrical conductivity of the material as shown in Fig 3a. The Seebeck coefficient measures the ability of a material to generate a voltage when subjected to a temperature gradient. With increasing Se vacancies, the Seebeck coefficient of $SnSe_2$ may change. The presence of defects alters the electronic band structure, leading to modifications in the energy levels available for charge carriers and affecting the Seebeck coefficient as shown in Fig 3b. The exact effect of Se vacancies on the Seebeck coefficient depends on the specific nature and concentration of the vacancies. A higher Seebeck coefficient indicates a larger voltage output for a given temperature difference, which can contribute to a higher power factor. However, the relationship between the Seebeck coefficient and power factor is not straightforward, as other factors such as electrical conductivity and thermal conductivity also come into play. Se vacancies also influence the carrier concentration and carrier mobility. Both of these factors have an impact on the power factor. An increase in carrier concentration, as facilitated by Se vacancies, can enhance the power factor by increasing the number of available charge carriers. Similarly, higher carrier mobility can lead to better electrical con-

DOI: 10.54227/mlab.20230023

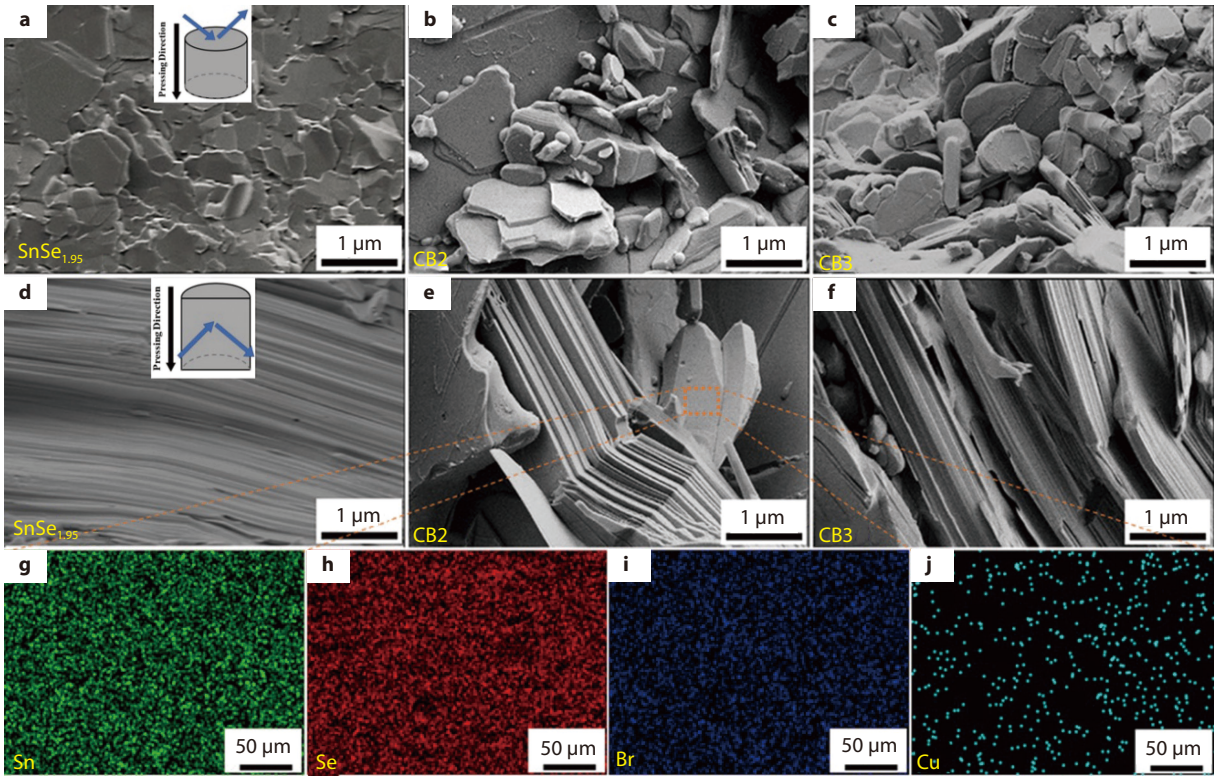


Fig. 2 FE-SEM images of the fresh fracture surfaces for the $Sn_{1-x}Cu_xSe_{1.95-y}Br_y$ samples along **a-c** perpendicular and **d-f** parallel directions to the pressing of SPS, **g-j** the EDX and the equivalent mappings for Sn, Se, and Br atoms of the representative doped compound ($Sn_{0.085}Cu_{0.015}Se_{1.92}Br_{0.03}$).

ductivity and improved power factor. $SnSe_2$ has low thermal conductivity as shown in Fig. 3c, which is crucial for efficient thermoelectric performance. Se vacancies can disrupt the crystal lattice and introduce scattering centers for heat-carrying phonons, resulting in an additional reduction in thermal conductivity. Therefore, increasing Se vacancies can potentially enhance the thermoelectric efficiency of $SnSe_2$ by further lowering its thermal conductivity.

It is noteworthy to acknowledge that the specific influence of selenium (Se) vacancies on the thermoelectric properties of $SnSe_2$ can vary depending on factors such as the concentration, distribution, and characteristics of these vacancies. Furthermore, the presence of Se vacancies can interact with other factors like doping or alloying with different elements, introducing additional complexities that impact the overall thermoelectric performance of $SnSe_2$. The effect of increasing Se vacancies on its *ZT* value, the impact can vary depending on the specific conditions and characteristics of the vacancies. Generally, increasing Se vacancies can lead to changes in the electrical conductivity, Seebeck coefficient, and thermal conductivity, as discussed earlier. The combined effect of these changes will ultimately determine whether the *ZT* value increases, decreases, or remains unchanged. Here, we can observe that $SnSe_{1.95}$ exhibits the highest *ZT* value, specifically in the perpendicular direction, as depicted in Fig. 3d. Therefore, this value will be utilized for the doped structure to further enhance the thermoelectric properties.

Thus far, our investigation has involved a comparative analysis of the electrical parameters of $SnSe_2$ and its variations in both parallel and perpendicular directions (refer to supporting data S3 for the parallel direction). This approach was undertaken to identify the optimum level of Sn enrichment and the direction of Spark Plasma Sintering (SPS) pressure that yield superior outcomes. Our results, depicted in Fig. 3a-d, unequivocally demonstrate that $SnSe_{1.95}$ exhibits the most promising properties in the perpendicular direction, surpassing all other samples. The implications of these findings extend beyond a comprehensive comprehension of the behavior of thermoelectric materials based on SnSe. They also hold significance in facilitating the design and optimization of more effective candidates and quantities of dopants for $SnSe_2$, thereby further enhancing its thermoelectric performance.

In the temperature range studied, most of the synthesized samples of $Sn_xCu_{1-x}Se_{1.95-y}Br_y$ ($0 \le x \le 0.035$ and $0 \le y \le 0.07$) exhibit semiconductor behavior and are thermally sensitive. In comparison to previous studies conducted by Kim et al. and Wu et al. with equivalent nominal doping content, larger values of electrical conductivity (σ) and Seebeck coefficient (S) have been observed[28, 46]. Moreover, the change in S is more significant than the change in σ, as shown in Fig. 4a, c. Therefore, the improvement in S can be attributed to the heavy doping of Br, while maintaining the semiconducting transport nature[47]. This increase in S is more advantageous than the increase in σ, as the thermoelectric efficiency is directly proportional to the power factor, which is represented by $S^2\sigma$. Therefore, the sample with $x = 0.015$ and $y = 0.03$ exhibits the highest power factor (PF) value up to 795 $\mu W\ m^{-1}\ K^{-2}$ in per-

DOI: 10.54227/mlab.20230023

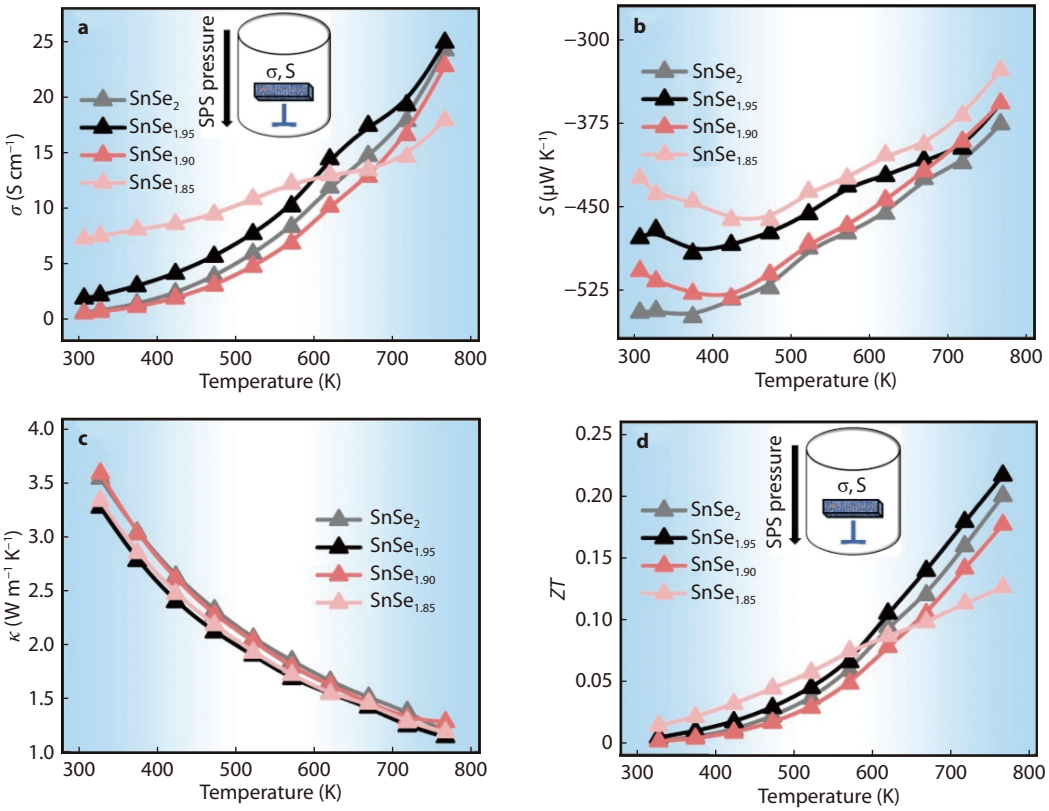


Fig. 3 Electrical transport properties for all the $SnSe_{2-x}$ (x = 0.05, 0.010, 0.15) samples, i.e. electrical conductivity, Seebeck coefficient as a function of temperature. **a, b** Thermal conductivity and *ZT* values as a function of temperature **c, d** along the perpendicular direction to SPS pressing.

pendicular direction, as illustrated in Fig. 4f, showing a significant enhancement of ~ 250% compared to pure $SnSe_{1.95}$ at 765 K. As the temperature increases beyond 400K, there is a noticeable decrease in the thermoelectric power factor, which is primarily attributed to a reduction in electrical conductivity (σ). The PF along the perpendicular direction increases vibrantly from 12.5 μW m^{-1} K^{-2} for pristine $SnSe_{1.95}$ to 255.7 μW m^{-1} K^{-2} for the $Sn_{0.985}Cu_{0.015}Se_{1.92}Br_{0.03}$ sample at 300 K, respectively. This behavior is similar to the conduct of electric conductivity versus temperature, thus PF for CB4 is smaller than that of CB2. For the transport properties for parallel direction refer to Fig. S4 of supporting data.

Band engineering has emerged as a promising strategy for enhancing the thermoelectric (TE) figure of merit (*ZT*) of materials. However, achieving a high *ZT* value is often a complex and daunting task owing to the interplay of competing factors that contribute to it. The *ZT* value is determined by several parameters, including the Seebeck coefficient, electrical conductivity, and thermal conductivity, which are strongly influenced by the charge carrier concentration (n) in a counterintuitive fashion. Consequently, optimal tuning of the carrier concentration is critical for maximizing the *ZT* value. In Fig. 4b, the Hall carrier concentration (n) and Hall mobility (μ) of $Sn_xCu_{1-x}Se_{1.95-y}Br_y$ ($0 \le x \le 0.035$ and $0 \le y \le 0.07$) at room temperature are presented as a function of doping concentration. The data reveals a uniform increase in n from 0.4 to 2.6 $\times 10^{18}$ cm^{-3} until CB3, followed by a significant increase. The observed carrier concentration is almost temperature-independent, indicating a degenerate conduction in the majority of samples by a single band, which agrees with electronic band structure calculations via DFT, as depicted in Fig. 6a-c. Using the relationship $\mu = \sigma/en$, where e is the elementary charge, the mobility (μ) is estimated and plotted as a function of doping content. The sample CB2 shows the highest mobility, which is attributed to its superior crystallinity in comparison to the other samples, as confirmed by XRD results in Fig. 1e. In contrast to n, μ decreases again beyond CB3, indicating an increase in the mean free path of the electron with decreased donor ionization energy, which behaves as a trap energy level of the scatters when x and y are lower than 0.015 and 0.03, respectively. The optimized carrier concentration, n_{opt} increases with increasing doping concentration, and the power factor also increases. The electrical conductivity (σ) of n-type doping exhibits a rapid increase as the carrier concentration rises, indicating a transition from semiconductor-like behavior to metal-like behavior. The power factor (PF), which is defined as the square of the Seebeck coefficient (S) multiplied by the electrical conductivity (σ), serves as a crucial parameter when searching for new thermoelectric materials with high output power. In the case of n-type Cu-Br co-doped $SnSe_{1.95}$, the dependence of PF on carrier concentration is illustrated in Fig. 4e, and it is observed that the maximum PF value corresponds to the optimal carrier concentration. Light electronic bands with small effective mass require a low content of dopants to optimize the power factor, while heavy band materials demand higher carrier

DOI: 10.54227/mlab.20230023

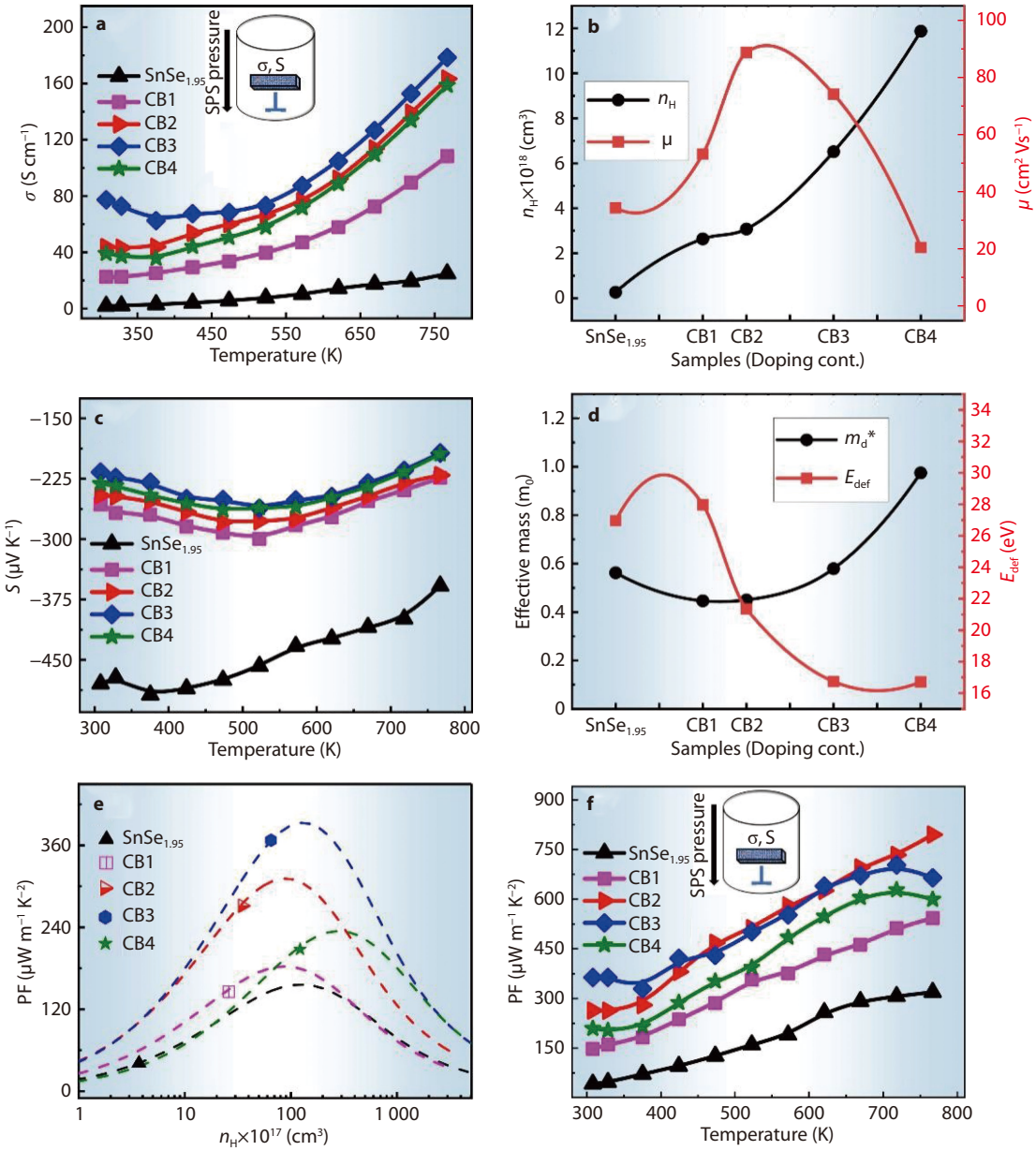


Fig. 4 Electrical transport properties for all the $Sn_{1-x}Cu_xSe_{1.95-y}Br_y$ samples along perpendicular direction. **a** Electrical conductivity. **b** Carrier concentration and mobility versus doping content. **c** Seebeck coefficient, as a function of temperature. **d** Effective mass and E_{def} versus doping content. **e** Power factor as a function of carrier concentration and **f** Power factor versus temperature.

concentrations. The PF values for CB3 reach the maximum at a carrier concentration of 12×10^{18} cm^{-3}.

Precise determination of the effective mass of the density of states (m_d*) holds paramount importance in the realm of thermoelectric materials research, as it enables the formulation of advanced strategies for material design and development. This is due to the temperature-dependent transport properties of these materials, which enable the computation of m_d* using the single parabolic model (SPB)[8]. The density of states effective mass (DOS) is a band parameter that primarily regulates the density of electronic states in a parabolic band. In the context of acoustic phonon scattering, the DOS effective mass is equivalent to the m_d* computed from *S* and *n*. Precise estimation of m_d* necessitates the fitting of the *n*-dependent *S* calculations to the SPB model, which is a complex numerical computation. Therefore, estimating m_d* using the SPB model is a complicated process that involves numerical calculations. Alternatively, a simple equation that interrelates *S*, *n*, and m_d* has been widely employed to estimate m_d*[45], $|s| = \frac{8\pi^2 k_b^2}{3eh^2}\left(\frac{\pi}{3n}\right)^{23} m^* T$. This equation must be used with caution as it is only valid for metals or degenerate semiconductors. Consequently, we have utilized this equation to obtain the effective mass of the $SnSe_2$-based samples. A significant increase in m_d* has been observed with the increase in Cu-Br doping, consistent with previously reported values[46], as demonstrated in Fig. 4d, which could potentially enhance the power factor optimization. Fig. 4d also depicts the vari-

DOI: 10.54227/mlab.20230023

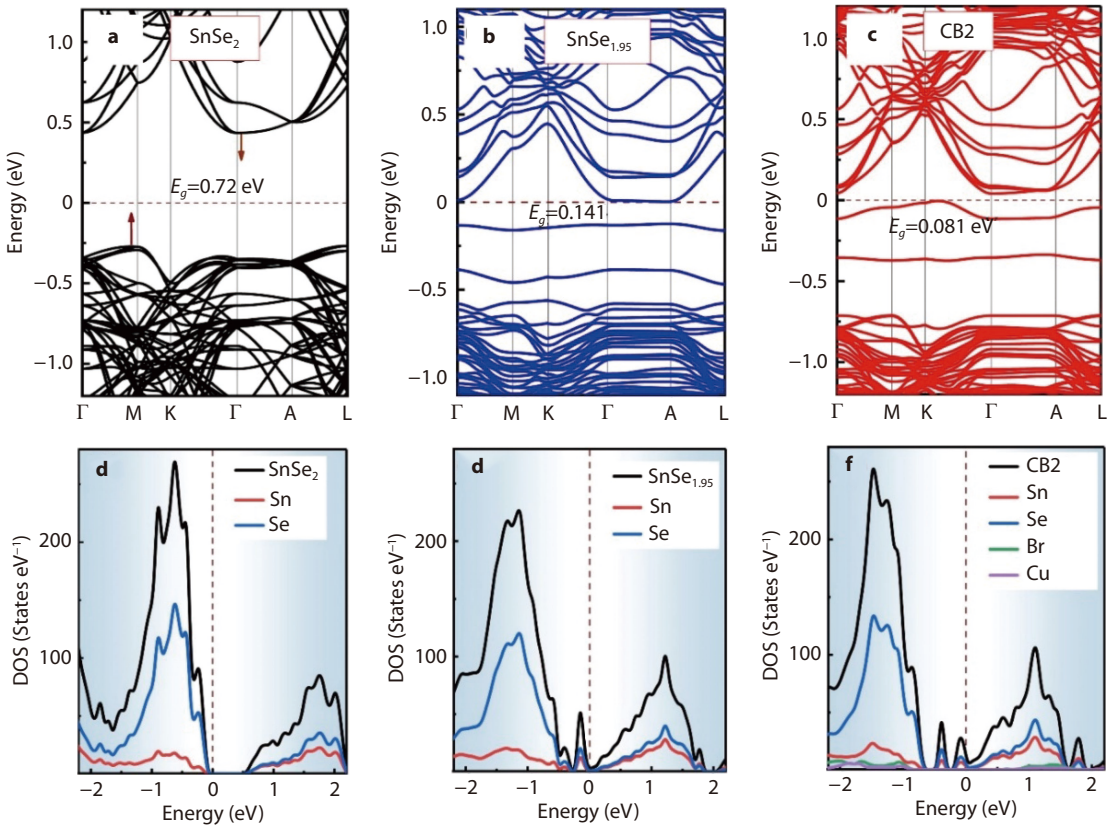


Fig. 5 **a-c** Electronic band structures for the $SnSe_2$, $SnS_{1.95}$ and CB2 crystal structures. **d-f** Total and projected density of states of the samples. The calculations have been done by DFT using VASP.

ation of deformation energy (E_{def}) as a function of Cu-Br doping level. The data reveals that the effective mass values exhibit an increasing trend with increasing doping content. In contrast, E_{def} shows a decreasing trend with increasing Cu-Br doping. These trends indicate a coupling between the Seebeck coefficient and electrical conductivity, which can potentially enhance the power factor of the material.

The electronic band structure of a material describes the arrangement and distribution of allowed energy levels, known as bands, for electrons within the material's solid lattice. It provides valuable insights into the material's electronic properties, such as its electrical conductivity, thermal conductivity, and thermoelectric behavior. The density of states (DOS) is a fundamental concept that quantifies the number of electronic states available within a specified energy range. It serves as a crucial measure for analyzing and understanding the electronic characteristics of a material. The band structure and density of states are essential tools for comprehending and predicting various properties and behaviors of materials at the electronic level. $SnSe_2$ has been found to possess a multi-valley electronic band structure akin to Bi_2Te_3[48], where the conduction band minimum (CBM) and the valence band maximum (VBM) have a degeneracy number of N = 6. The high valley degeneracy results in a potentially high density-of-states effective mass (m^*_d)[49], which in turn leads to low thermal conductivity[25, 50]. In this study case, we used first-principles calculations to investigate the effect of Cu and Br co-doping on the electronic properties of Sn-rich $SnSe_2$. Fig. 5a shows that pure $SnSe_2$ is an indirect semiconductor with a bandgap of 0.72 eV, consistent with previous experimental studies[28]. The conduction band minima (CBM) bandwidth is wider than that of the valence band maxima (VBM), indicating that n-type conduction is more advantageous than p-type conduction in $SnSe_2$, as evidenced by the negative S values. We found that the enrichment of Sn caused decrease in the bandgap and introduction of Cu and Br on Sn and Se sites respectively, caused further decrease in the bandgap, which is the energy difference between the CBM and VBM as shown in Fig. 5b, c. The increase in thermoelectric performance can be attributed to the creation of additional electronic states within the bandgap by the substituted atoms. These additional states effectively lower the energy required for electron transitions from the valence band to the conduction band. Furthermore, our observations revealed an increase in band degeneracy in the Sn-rich and doped materials, resulting in an increased effective mass of the density of states. The effective mass refers to the apparent mass of an electron within a crystal, influenced by its interactions with the surrounding atoms. The effective mass is associated with the curvature of the electronic bands near the Fermi level, and a larger effective mass typically corresponds to a higher Seebeck coefficient. In doped semiconductors, the Fermi level shifts either towards the conduction band or the valence band, depending on the type of doping, in order to maintain charge neutrality. In the case of $SnSe_{1.95}$, the observed shift of the Fermi level towards the conduction band indicates the presence of holes result-

DOI: 10.54227/mlab.20230023

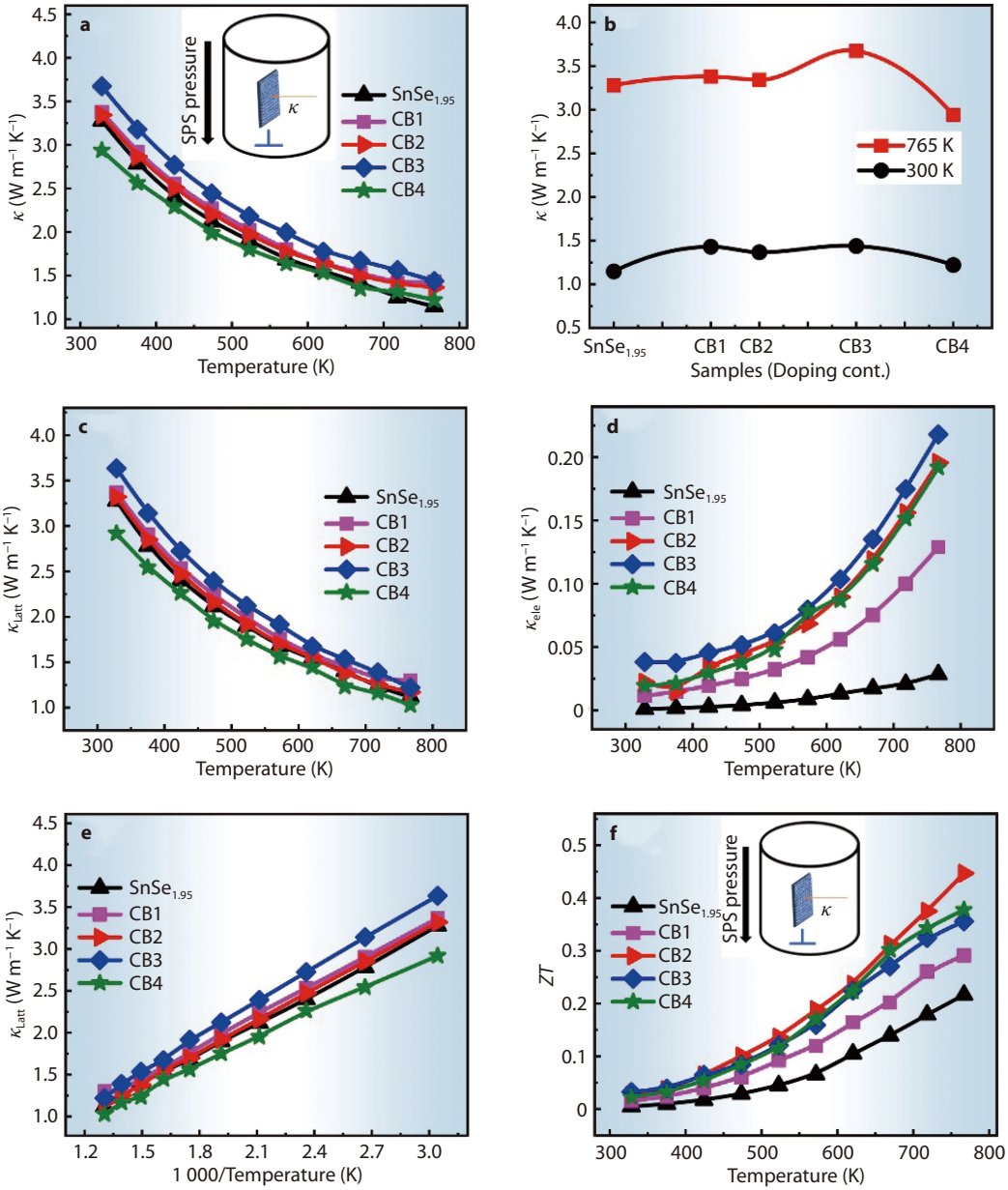


Fig. 6 Thermal conductivity for all the pure and Br-doped samples along the perpendicular direction to the SPS pressure. **a** and **b** Total thermal conductivity, as a function of temperature and doping content. **c** Lattice thermal and **d** electrical thermal conductivity as a function of temperature, respectively. **e** Lattice thermal conductivity as a function of 1000/temperature and **f** *ZT* values as a function of Temperature.

ing from the transfer of electrons from the Br atoms. The high degree of band degeneracy of n-type $SnSe_2$ is significant because it suggests that there is room for further optimization of this material for thermoelectric applications. Additionally, Fig. 5e-f provides plots of the total and projected electronic density of states (DOS and PDOS) for all relevant structures. These diagrams clearly illustrate that the Fermi level has shifted towards the conduction band, which is a common feature of doped semiconductors. This shift is essential for maintaining charge neutrality and conserving the number of particles, and it occurs here due to the transfer of electrons from Cu and Br atoms, which generates holes. It is known that the Seebeck coefficient (S) is directly proportional to the variation in density of states with respect to energy at the Fermi level. The asymmetry in the DOSs near the Fermi level is relatively uniform for most doping concentrations, and as a result, the variation in S is not significant despite the significant change in carrier concentration. The reduction in the bandgap of $SnSe_2$ to 0.081 eV after Br and Cu co-doping as shown Fig. 5c can be attributed to the introduction of impurity states within the bandgap. The incorporation of Br and Cu atoms into the $SnSe_2$ crystal lattice creates additional electronic states, leading to a modification of the electronic band structure. This modification results in a narrower bandgap compared to pristine $SnSe_2$. The phenomenon of bipolar diffusion, where both electrons and holes contribute to electrical conduction, can occur in materials with a narrow bandgap. When the bandgap is reduced, the energy barrier for elec-

DOI: 10.54227/mlab.20230023

tron-hole pair formation decreases, enabling the simultaneous movement of electrons and holes, leading to bipolar diffusion[51]. As for the thermal conductivity, it is important to note that in the case of $SnSe_2$, the reduction in bandgap alone may not directly influence the thermal conductivity. The thermal conductivity of a material depends on various factors such as lattice vibrations and phonon scattering mechanisms. While the bandgap narrowing may affect the electronic properties and charge transport, it does not necessarily result in a significant change in thermal conductivity. This indicates that the material's thermoelectric properties may not be drastically affected by changes in doping concentration, making it a promising candidate for use in thermoelectric devices.

Fig. 6 presents thermal conductivity curves with respect to temperature in the perpendicular direction, indicating a linear relationship between temperature and both total thermal conductivity (κ) and lattice thermal conductivity (κ_{Latt}) for all Cu-Br co-doped samples. Both κ_{Latt} and κ decrease significantly with increasing temperature for all samples. The electronic thermal conductivity (κ_{ele}) is much lower than κ_{Latt}, and the lattice thermal conductivity is almost equal to the total thermal conductivity, suggesting that phonons contribute significantly to thermal transport. These effects lead to lower lattice thermal conductivity in doped samples. Previous studies have indicated that the thermal conductivity of $SnSe_2$ is primarily dependent on phonon conduction. The reduction in thermal conductivity observed in Cu-Br co-doped $SnSe_{1.95}$ is attributed to the dopant-related alteration in the phonon spectra, which provides a new avenue for phonon engineering of polycrystalline TE materials. The impact of electronic thermal conductivity is minimal due to the smaller values of electrical conductivity. As the temperature increases, the average free path of phonons in the lattice decreases, resulting in a reduction in thermal conductivity. The thermal conductivity curves versus temperature in the perpendicular direction exhibit a nearly linear dependence on temperature and decrease significantly with increasing temperature for all Cu-Br co-doped samples. In Fig. 6e, the 1000/Temperature-dependent lattice thermal conductivity of $Sn_{1-x}Cu_xSe_{1.95-y}B_y$ (where x = 0, 0.01, 0.015, 0.025, 0.035 and y = 0.02, 0.03, 0.05, 0.07) is plotted along the perpendicular direction of SPS pressure. The linear relationship observed in the figure suggests that the Umklapp phonon scattering phenomenon dominates the scattering of phonons[52, 53]. In the supporting information S5, it is evident that there is a substantial difference between the values of total thermal conductivity in both directions, especially for the doped structures. The observed significant difference in thermal conductivity between the two directions indicates a strong anisotropy between them.

The ZT values for all samples of $Sn_{1-x}Cu_xSe_{1.95-y}B_y$ (where x = 0, 0.01, 0.015, 0.025, 0.035 and y = 0, 0.02, 0.03, 0.05, 0.07) were estimated by utilizing the measured values of σ, S, and κ, and plotted in Fig. S5 and Fig. 6f for both parallel and perpendicular directions, respectively. The results demonstrate that the ZT along the perpendicular direction is greater than that along the parallel direction, and this difference increases with the level of Cu-Br co-doping, indicating a strong anisotropy. The ZT values exhibit notable improvement as a result of increasing Cu-Br doping, primarily attributed to the enhancement of the power factor, as illustrated in Fig. 4f. Specifically, for CB2, the maximum ZT value of 0.46 in the perpendicular direction was achieved at 765 K, representing an approximately 2.5-fold increase compared to pure $SnSe_{1.95}$ (ZT = 0.19). This finding suggests that co-doping in the perpendicular direction yields superior thermoelectric performance. Conversely, in the parallel direction, the ZT value for the same doping and temperature is significantly lower, specifically 0.3. Our investigations have found that the optimization of carrier concentration through the co-doping of Cu and Br upon Sn-rich $SeSe_2$ can significantly enhance the ZT value. The highest ZT value of 0.46 at 748 K for the CB2 sample is more significant than most reported single and polycrystalline $SnSe_2$[36, 37, 54] at the same temperature range, including those that were Br-doped, Br-co-doped and Br-doped combined with intercalated Cu in layers. [28, 46]

Conclusions

$SnSe_2$ has emerged as a promising thermoelectric material due to its desirable attributes such as excellent thermal stability and low toxicity. However, its inherent poor thermoelectric performance has hindered its practical applications. To address this limitation, we have devised a novel approach in this study, combining mechanical alloying (MA) and spark plasma sintering (SPS) techniques, to synthesize n-type Sn-rich Cu-Br co-doped $SnSe_2$ polycrystals. Through careful optimization of the substitutional doping process, we have achieved an optimized material for further enhancements. The introduction of co-doping has resulted in a significant increase in carrier concentration, thereby greatly improving the thermoelectric performance of $SnSe_2$. Notably, the power factor, which quantifies the combination of electrical conductivity and Seebeck coefficient, has been increased to approximately 795 $\mu W\ m^{-1}\ K^{-2}$ at 765 K, primarily attributed to the Cu-Br co-doping. Density functional theory (DFT) calculations have been employed to investigate the electronic band structure and density of states, revealing a reduced bandgap and increased degeneracy. These findings provide theoretical support for the observed enhancement in the thermoelectric properties of the Cu-Br co-doped Sn-rich $SnSe_2$ polycrystals. Finally, we have achieved a maximum figure of merit (ZT) value of 0.46 at 765 K for the $Sn_{0.985}Cu_{0.015}Se_{1.92}Br_{0.03}$ sample, measured perpendicular to the SPS pressing direction. This value is nearly three times higher than that of pure $SnSe_{1.95}$, clearly demonstrating the improved thermoelectric performance achieved through co-doping of $SnSe_2$ polycrystals.

■ ACKNOWLEGEMENTS

This work is supported by the Technology Plan Project of Shenzhen (20220810154601001, JCYJ20220531103601003), National Natural Science Foundation of China (No. 62274112).

■ CONFLICT OF INTEREST

The authors declare no conflict of interest

■ AUTHOR CONTRIBUTIONS

The idea was conceived by M. Nisar, who also analyzed the results and took the lead in writing the paper. The synthesis and characterization of the samples were carried out by W.

DOI: 10.54227/mlab.20230023

Qin. Transport properties measurements were performed by J. Zhang, Z. Zheng, and Fu Li. G. Liang, P. Fan, and Y.-X. Chen contributed to the manuscript by engaging in discussions, providing edits, and offering valuable comments.

■ REFERENCES

1. G. J. Snyder, E. S. Toberer, *Nature Materials*, 2008, 7, 105
2. D. M. Rowe, *Renewable Energy*, 1999, 16, 1251
3. J. Choi, Y. Jung, S. J. Yang, J. Y. Oh, J. Oh, K. Jo, J. G. Son, S. E. Moon, C. R. Park, H. Kim, *ACS Nano*, 2017, 11, 7608
4. J. Jung, E. H. Suh, Y. J. Jeong, H. S. Yang, T. Lee, J. Jang, *ACS Applied Materials & Interfaces*, 2019, 11, 47330
5. J. S. Son, H. Zhang, J. Jang, B. Poudel, A. Waring, L. Nally, D. V. Talapin, *Angewandte Chemie International Edition*, 2014, 53, 7466
6. S. Jo, S. H. Park, H. W. Ban, D. H. Gu, B.-S. Kim, J. H. Son, H.-K. Hong, Z. Lee, H.-S. Han, W. Jo, J. E. Lee, J. S. Son, *Journal of Alloys and Compounds*, 2016, 689, 899
7. Y. Zhang, Y. Chen, C. Gong, J. Yang, R. Qian, Y. Wang, *Journal of Microelectromechanical Systems*, 2007, 16, 1113
8. H. J. Goldsmid, The Physics of Thermoelectric Energy Conversion, *Morgan & Claypool Publishers*, America, 2017.
9. A. D. LaLonde, Y. Pei, H. Wang, G. Jeffrey Snyder, *Materials Today*, 2011, 14, 526
10. J. R. Sootsman, D. Y. Chung, M. G. Kanatzidis, *Angewandte Chemie International Edition*, 2009, 48, 8616
11. Z. Yu, X. Wang, C. Liu, Y. Cheng, Z. Zhang, R. Si, X. Bai, X. Hu, J. Gao, Y. Peng, L. Miao, *Journal of Advanced Ceramics*, 2022, 11, 1144
12. Z.-H. Zheng, D.-L. Zhang, B. Jabar, T.-B. Chen, M. Nisar, Y.-F. Chen, F. Li, S. Chen, G.-X. Liang, X.-H. Zhang, P. Fan, Y.-X. Chen, *Materials Today Physics*, 2022, 24, 100659
13. Z.-G. Chen, X. Shi, L.-D. Zhao, J. Zou, *Progress in Materials Science*, 2018, 97, 283
14. S. Singh, S. Lee, H. Kang, J. Lee, S. Baik, *Energy Storage Materials*, 2016, 3, 55
15. Y. Sadia, Z. Aminov, D. Mogilyansky, Y. Gelbstein, *Intermetallics*, 2016, 68, 71
16. G. Tan, L.-D. Zhao, M. G. Kanatzidis, *Chemical Reviews*, 2016, 116, 12123
17. Q. Zhang, B. Liao, Y. Lan, K. Lukas, W. Liu, K. Esfarjani, C. Opeil, D. Broido, G. Chen, Z. Ren, *Proceedings of the National Academy of Sciences*, 2013, 110, 13261
18. L. D. Hicks, M. S. Dresselhaus, *Physical Review B*, 1993, 47, 12727
19. M. Christensen, A. B. Abrahamsen, N. B. Christensen, F. Juranyi, N. H. Andersen, K. Lefmann, J. Andreasson, C. R. H. Bahl, B. B. Iversen, *Nature Materials*, 2008, 7, 811
20. Y. Liu, W. Wang, J. Yang, S. Li, *Advanced Sustainable Systems*, 2018, 2, 1800046
21. M. Samanta, T. Ghosh, S. Chandra, K. Biswas, *Journal of Materials Chemistry A*, 2020, 8, 12226
22. F. Guo, B. Cui, H. Geng, Y. Zhang, H. Wu, Q. Zhang, B. Yu, S. J. Pennycook, W. Cai, J. Sui, *Small*, 2019, 15, 1902493
23. L. Xie, D. He, J. He, *Materials Horizons*, 2021, 8, 1847
24. W. He, D. Wang, H. Wu, Y. Xiao, Y. Zhang, D. He, Y. Feng, Y.-J. Hao, J.-F. Dong, R. Chetty, L. Hao, D. Chen, J. Qin, Q. Yang, X. Li, J.-M. Song, Y. Zhu, W. Xu, C. Niu, X. Li, G. Wang, C. Liu, M. Ohta, S. J. Pennycook, J. He, J.-F. Li, L.-D. Zhao, *Science*, 2019, 365, 1418
25. B.-Z. Sun, Z. Ma, C. He, K. Wu, *Physical Chemistry Chemical Physics*, 2015, 17, 29844
26. F. Li, Z. Zheng, Y. Li, W. Wang, J.-F. Li, B. Li, A. Zhong, J. Luo, P. Fan, *Journal of Materials Science*, 2017, 52, 10506
27. Y. Luo, Y. Zheng, Z. Luo, S. Hao, C. Du, Q. Liang, Z. Li, K. A. Khor, K. Hippalgaonkar, J. Xu, Q. Yan, C. Wolverton, M. G. Kanatzidis, *Advanced Energy Materials*, 2018, 8, 1702167
28. Y. Wu, W. Li, A. Faghaninia, Z. Chen, J. Li, X. Zhang, B. Gao, S. Lin, B. Zhou, A. Jain, Y. Pei, *Materials Today Physics*, 2017, 3, 127
29. G. Li, G. Ding, G. Gao, *Journal of Physics:Condensed Matter*, 2017, 29, 015001
30. Z. Fang, S. Hao, L. Long, H. Fang, T. Qiang, Y. Song, *CrystEngComm*, 2014, 16, 2404
31. P. Yu, X. Yu, W. Lu, H. Lin, L. Sun, K. Du, F. Liu, W. Fu, Q. Zeng, Z. Shen, C. Jin, Q. J. Wang, Z. Liu, *Advanced Functional Materials*, 2016, 26, 137
32. L.-D. Zhao, S.-H. Lo, Y. Zhang, H. Sun, G. Tan, C. Uher, C. Wolverton, V. P. Dravid, M. G. Kanatzidis, *Nature*, 2014, 508, 373
33. Y. Qin, T. Xiong, J.-f. Zhu, Y.-l. Yang, H.-r. Ren, H.-l. He, C.-p. Niu, X.-h. Li, M.-q. Xie, T. Zhao, *Journal of Advanced Ceramics*, 2022, 11, 1671
34. Y. Zhang, Y. Liu, K. H. Lim, C. Xing, M. Li, T. Zhang, P. Tang, J. Arbiol, J. Llorca, K. M. Ng, M. Ibáñez, P. Guardia, M. Prato, D. Cadavid, A. Cabot, *Angewandte Chemie International Edition*, 2018, 57, 17063
35. C. Liu, Z. Huang, D. Wang, X. Wang, L. Miao, X. Wang, S. Wu, N. Toyama, T. Asaka, J. Chen, E. Nishibori, L.-D. Zhao, *Journal of Materials Chemistry A*, 2019, 7, 9761
36. A.-T. Pham, T. H. Vu, Q. V. Nguyen, M. T. Vu, J. H. Park, S.-D. Park, S. Cho, *ACS Applied Energy Materials*, 2021, 4, 2908
37. C. Zhou, Y. Yu, X. Zhang, Y. Cheng, J. Xu, Y. K. Lee, B. Yoo, O. Cojocaru-Mirédin, G. Liu, S.-P. Cho, M. Wuttig, T. Hyeon, I. Chung, *Advanced Functional Materials*, 2020, 30, 1908405
38. P. Xu, T. Fu, J. Xin, Y. Liu, P. Ying, X. Zhao, H. Pan, T. Zhu, *Science Bulletin*, 2017, 62, 1663
39. M. Nisar, Y.-X. Chen, W. Qin, A. Abbas, Z. Zheng, P. Fan, F. Li, *Journal of Alloys and Compounds*, 2023, 959, 170566
40. H. Wiedemeier, G. Pultz, U. Gaur, B. Wunderlich, *Thermochimica Acta*, 1981, 43, 297
41. G. Kresse, J. Furthmüller, *Computational Materials Science*, 1996, 6, 15
42. G. Kresse, J. Furthmüller, *Physical Review B*, 1996, 54, 11169
43. G. Kresse, D. Joubert, *Physical Review B*, 1999, 59, 1758
44. J. P. Perdew, K. Burke, M. Ernzerhof, *Physical Review Letters*, 1996, 77, 3865
45. J. P. Perdew, K. Burke, M. Ernzerhof, *Physical Review Letters*, 1997, 78, 1396
46. S.-i. Kim, J. Bang, J. An, S. Hong, G. Bang, W. H. Shin, T. Kim, K. Lee, *Journal of Alloys and Compounds*, 2021, 868, 159161
47. B. A. MacLeod, N. J. Stanton, I. E. Gould, D. Wesenberg, R. Ihly, Z. R. Owczarczyk, K. E. Hurst, C. S. Fewox, C. N. Folmar, K. Holman Hughes, B. L. Zink, J. L. Blackburn, A. J. Ferguson, *Energy & Environmental Science*, 2017, 10, 2168
48. T. Fang, X. Li, C. Hu, Q. Zhang, J. Yang, W. Zhang, X. Zhao, D. J. Singh, T. Zhu, *Advanced Functional Materials*, 2019, 29, 1900677
49. Y. Pei, H. Wang, G. J. Snyder, *Advanced Materials*, 2012, 24, 6125
50. Y. Ding, B. Xiao, G. Tang, J. Hong, *The Journal of Physical Chemistry C*, 2017, 121, 225
51. Y. Shu, X. Su, H. Xie, G. Zheng, W. Liu, Y. Yan, T. Luo, X. Yang, D.

DOI: 10.54227/mlab.20230023

Yang, C. Uher, X. Tang, *ACS Applied Materials & Interfaces*, 2018, 10, 15793
52. Y.-X. Chen, Z.-H. Ge, M. Yin, D. Feng, X.-Q. Huang, W. Zhao, J. He, *Advanced Functional Materials*, 2016, 26, 6836
53. X. Shi, A. Wu, W. Liu, R. Moshwan, Y. Wang, Z.-G. Chen, J. Zou, *ACS Nano*, 2018, 12, 11417
54. L. Cai-Yun, H. Wen-Ke, W. Dong-Yang, Z. Xiao, Z. Li-Dong, *Acta Physica Sinica*, 2021, 70, 208401



©2024 The Authors. *Materials Lab* is published by Lab Academic Press. This is an open access article under the terms of the Creative Commons Attribution License, which permits use, distribution and reproduction in any medium, provided the original work is properly cited.